Phenomenological Understanding of Hematite Photoanode Performance

João Pina,* Paula Dias,* Carlos Serpa, João Azevedo, Adélio Mendes, and João Sérgio Seixas de Melo

Read Online

ACCESS | Metrics & More | Article Recommendations | Supporting Information

ABSTRACT: The effect of the structural and electronic properties of hematite photoanodes on the charge carrier dynamics was investigated by photoelectrochemistry and transient absorption spectroscopy (TAS). Hematite photoelectrodes were prepared by spray pyrolysis and hydrothermal methods for obtaining films with different thicknesses, morphologies, doping agents, and surface treatments. TAS analyses were performed using standalone photoelectrodes, a three-electrode configuration and in operando. TAS studies revealed that there is a significant electron−hole recombination within the first few hundred picoseconds and smaller amplitude of longer-lived charge carriers, which are responsible for the generated photocurrent observed in photoelectrochemical measurements. The best performing photoelectrodes are Sn-doped hematite thin film annealed at 800 °C and coated with IrO_2/RuO_2 co-catalyst and the Ti-doped hematite nanowires. The effect of surface treatments, *i.e.*, high-temperature annealing responsible for Sn intrinsic doping and co-catalyst coating, on the electron−hole recombination dynamics is negligible at the picosecond time scale. The TAS studies showed a slower electron−hole recombination after Ti incorporation, increased electron density, and enlarged surface area.

1. INTRODUCTION

Hematite (α-Fe_2O_3) photoelectrode is widely studied for photoelectrochemical (PEC) water splitting cells, showing a favorable combination of low price, abundance, nontoxicity, narrow bandgap of *ca.* 2.1 eV, and excellent chemical stability in neutral and basic aqueous solutions.[1,2] However, the maximum photocurrent density reported to date with a hematite photoelectrode is half of its theoretical limit of *ca.* 12.6 mA·cm^{-2}.[3] Recently, hematite photoelectrodes have also created interest for solar charging redox flow batteries—solar redox flow cells[4]—but, in spite of the fast redox kinetics of potassium ferrocyanide ($K_4Fe(CN)_6$), the performance is still far from the theoretical limit.[5,6] The limitations hindering the hematite efficiency are: (i) low charge separation efficiency, which results from its very short excited-state lifetime (3−10 ps) and hole diffusion length (2−4 nm); (ii) low absorption coefficient, requiring 400−500 nm thick films for complete light absorption; (iii) poor oxygen evolution reaction kinetics; and (iv) low electrical conductivity (*ca.* 10^{-14} Ω^{-1}·cm^{-1}).[7] Indeed, hematite modest oxygen evolution reaction kinetics and its poor efficiency in delivering photogenerated holes, especially holes generated by photoexcitation, to the electrode−electrolyte interface are obstacles to be overcome. The low charge separation efficiency, mainly for charge carriers generated in the bulk of thick films, leads to significant electron−hole recombination losses on timescales ranging from picoseconds to milliseconds.[2] Extreme doping, reduction

of film thickness, morphology control (*e.g.*, nanostructuring), surface passivation using overlayers and co-catalysts, and incorporation of electron collecting scaffolds are some approaches considered to overcome these shortcomings.[2]

Understanding the dynamics of charge carrier processes is crucial for improving the PEC performance of hematite photoelectrodes by reducing charge carrier trapping and recombination phenomena. While electrochemical techniques such as impedance spectroscopy (EIS) and intensity-modulated photocurrent/photopotential spectroscopy (IMPS/IMVS) are mainly employed to study the kinetics of PEC water splitting cells,[1,8,9] these frequency domain techniques are limited as they only monitor the extraction of photogenerated electrons traveling from the photoelectrode to the external circuit, *i.e.*, they are used to investigate the physical−chemical processes. EIS is used to investigate the dynamic relation between photocurrent and photopotential, whereas the relation between irradiation and the electrochemical response is studied using IMPS/IMVS tools. In
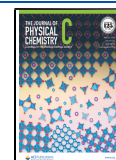
contrast, transient absorption spectroscopy (TAS) is a useful, nondestructive, analytical tool to monitor the absorption and concentration of photogenerated charge carriers over time, thus providing insights into the mechanisms of both electrons and holes.[2]

Several TAS studies have been reported to investigate the recombination dynamics and understand how lifetimes of both photoexcited charge carriers vary in hematite photoelectrodes from thin films to nanostructures,[2,10] as well as using dopant agents[11] and co-catalysts.[12] For mimicking the environment of a PEC cell, an external bias potential can be also applied to the hematite films.[12] Nevertheless, much is still unknown about hematite photoanodes, especially with regard to the relationship between the electronic structure, excited-state dynamics, and photoelectrochemical performance.

2. MATERIALS AND METHODS

Hematite planar thin films were prepared by spray pyrolysis, while the hematite nanowires (NWs) were synthesized using a hydrothermal method, following the work of Vayssieres et al.[13] A complete description of the preparation methods can be found in the Supporting Information (SI).

The hematite photoelectrodes were photoelectrochemically characterized using the PEC cell device known as "cappuccino",[14] in a standard three-electrode configuration (see the Supporting Information for details).

Transient absorption measurements in the femtosecond to nanosecond and nanosecond to microsecond ranges were performed in a HELIOS spectrometer from Ultrafast Systems[15] and in an Applied Photophysics laser flash photolysis apparatus,[16] respectively. Modifications of the TAS spectrometers sample holders were necessary to probe the samples in operando conditions. A complete description of the experimental procedure can be found in Supporting Information.

3. RESULTS AND DISCUSSION

3.1. Photoelectrochemical Measurements (J–V Characteristic Curves). Several batches of hematite photoelectrodes were prepared to investigate the relation among their structural, morphological, and surface properties on the photoelectrochemical and optoelectronic performances, namely, on the hematite photogenerated charge transfer kinetics (on the bulk and surface properties). Table 1 presents a description of all of the prepared hematite samples according to the parameter under study:

(a) film thickness—bare hematite planar thin films prepared by spray pyrolysis (coded as SP samples) depositing different volumes of 10 mM $Fe(acac)_3$ precursor solution (V), V = 30, 42, and 60 mL, which allows achieving film thicknesses of ca. 13, 19, and 24 nm, respectively (hereafter coded as SP-13, SP-19, and SP-24 samples);

(b) morphology—hematite planar thin films prepared by spray pyrolysis annealed at 800 °C (coded as SP-800 sample), and nanostructured films (nanowires) prepared by hydrothermal method with a thickness of ca. 400 nm (coded as NW-800 sample);

(c) surface passivation—(i) high-temperature annealing at 800 °C (coded as SP-800 sample) and (ii) activation with efficient co-catalysts, such as IrO_2/RuO_2 (coded as

Table 1. Description of the Prepared Hematite Photoelectrodes

sample code	sample description
	Reference Sample
SP-19	SP deposited with a film thickness of ca. 19 nm
	Film Thickness
SP-13	SP with a film thickness of ca. 13 nm
SP-24	SP with a film thickness of ca. 24 nm
	Morphology
SP-800	SP-19 sample with an annealing treatment at 800 °C
NW-800	NW with a film thickness <400 nm and annealed at 800 °C
	Surface Passivation with Co-Catalysts
SP-800-IrO_2RuO_2	SP-800 sample coated with IrO_2/RuO_2 co-catalysts
SP-NiFeOOH	SP-19 sample coated with $NiFeO_x$ co-catalyst
	Doping
SP-800	SP-19 sample with an annealing treatment at 800 °C—in situ Sn doping
SP-Si	SP-19 sample ex situ doped with 3% Si
NW-Ti	NW-800 sample ex situ doped with Ti

SP-800-IrO_2RuO_2 sample) and NiFeOOH (coded as SP-NiFeOOH sample);

(d) doping—incorporation of ion impurities of Sn (in situ doping of hematite thin film, promoted by the Sn^{4+} migration from the fluorine-doped tin oxide (FTO) layer after annealing at 800 °C), Si (ex situ doping of hematite thin film, adding 3% Si^{4+}), and Ti (ex situ doping of hematite nanostructured film, adding 1.5 mM $Ti(OBu)_4$), hereafter coded as SP-800, SP-Si, and NW-Ti samples, respectively.

Figure 1 shows the $J–V$ characteristic curves obtained for all of the prepared samples, organized by the four parameters under study and evaluated in a three-electrode configuration, using 1 M NaOH as an electrolyte solution. The hematite thin film prepared by spray pyrolysis with ca. 19 nm (SP-19) was used as a reference sample.

The first parameter tested and identified as critical for the performance of a hematite thin film was the film thickness (directly influenced by the amount of deposited precursor solution). The hematite thickness was estimated using a UV–visible absorption spectrometer, and assuming a Lambertian absorption behavior, as reported elsewhere.[3] The $J–V$ characteristic curves obtained in the dark and under simulated sunlight are shown in Figure 1a.

From Figure 1a, it can be observed that the generated photocurrent density varies with the thickness of the hematite thin films, since it influences the amount of absorbed light from the semiconductor. The bare hematite thin film with ca. 19 nm thickness (SP-19 sample) reached the maximum photocurrent density of ca. 0.81 mA·cm^{-2} at 1.45 V_{RHE} (applied potential bias reported as a function of the reversible hydrogen electrode, RHE). Samples SP-13 and SP-24 (with thicknesses of ca. 13 and 24 nm, respectively) showed lower photocurrents of ca. 0.65 and 0.68 mA·cm^{-2} at 1.45 V_{RHE}, respectively. As previously demonstrated by Dias et al.,[3] a planar thin film of ca. 19 nm, displaying good homogeneity and a conformal coating of the FTO-glass substrate, has the suitable thickness for suppressing the charge transport limitation of hematite and minimizing the bulk recombination losses. The literature also reports that a hematite planar film thickness of ca. 20 nm maximizes the internal quantum yield.[17]
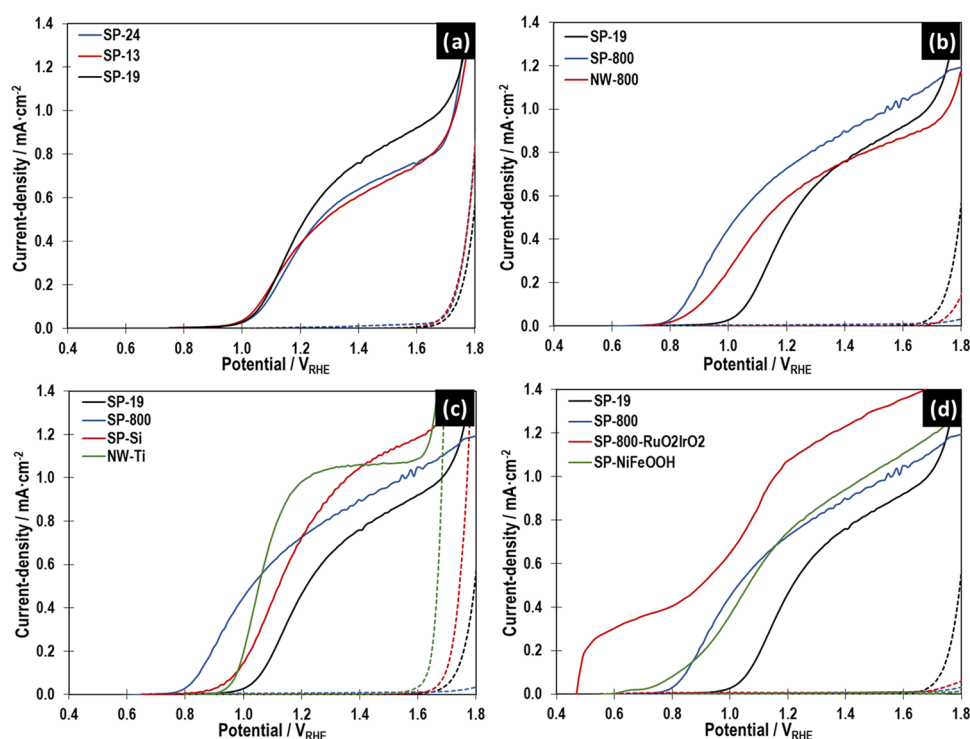
Figure 1. $J-V$ characteristics of the prepared hematite photoelectrodes, obtained in the dark (dashed lines) and under 1-sun AM 1.5 G irradiation (solid lines) conditions, for comparing the parameters under study: (a) film thickness, (b) morphology, (c) doping, and (d) surface passivation.

However, the PEC activity of the SP-19 sample is mainly limited by recombination of holes at the hematite surface and its small light absorption. Annealing at high temperatures (800 °C) was performed to improve the film crystallinity and charge carrier extraction.[18] Moreover, the hematite photoelectrodes sintered above 650 °C promotes the diffusion of Sn from the FTO layer, which contributes to an *in situ* Sn doping responsible for the observed photocurrent enhancement (Figure 1b). The SP-800 sample showed then a 15% current increase and a cathodic shift of *ca*. 200 mV in the onset potential (0.80 V_{RHE}). For improving the light absorption, while maintaining a short charge carrier collection length, nanostructured hematite films were prepared using a solution-based method followed by annealing at 800 °C over 20 min (NW-800 sample). This technique allows obtaining hematite nanowires (NW) with thicknesses of *ca*. 285 and 379 nm before and after the annealing treatment at 800 °C (see Table S1 in the Supporting Information). Despite presenting a higher surface area, the NW-800 sample showed a similar photocurrent at 1.45 V_{RHE} compared with the SP-19 sample (Figure 1b). This can be related to the poor conduction of the majority charge carriers (electrons) to the FTO back contact, which hinders the efficiency of thick hematite photoelectrodes.

The limited carrier conductivity of hematite was overcome by doping with transition metals, such as Ti, Si, and Sn dopants, for enhancing the photocurrent in hematite photoelectrodes.[19−23] Hematite nanowires doped with Ti impurities (NW-Ti sample) presented a lower thickness than the NW-800 sample (*ca*. 335 nm—Table S1), which allows a performance improvement of >25% (photocurrent density of *ca*. 1.06 mA·cm^{-2} at 1.45 V_{RHE})—Figures 1c and S3. Despite both NW samples (NW-800 and NW-Ti) presented an onset potential of photocurrent at *ca*. 0.90 V_{RHE}, the NW-Ti sample showed a steeper increase and saturation at lower potentials

that culminated in a better fill factor (resulting in similar performances at 1.23 and 1.45 V_{RHE}). The comparison between planar thin films intrinsically doped with Sn (SP-800) and nanowired films doped with Ti (NW-Ti) showed a more cathodic onset potential (*ca*. 0.80 V_{RHE}) for the SP-800 sample due to the surface passivation through the annealing of hematite thin films at 800 °C, whereas the NW-Ti sample showed an improved fill factor that is attributed not only to the enlarged surface area but also to the increased donor density and shortened transport distance of the photogenerated holes to the surface.[24] Elemental *ex situ* doping in hematite thin films with 3% Si (SP-Si) was also studied; Figure 1c shows a photocurrent increase of 30 and 15% comparing the SP-Si sample with the SP-19 and SP-800 samples, respectively, showing that Si-doping is more effective in improving the PEC efficiency, mainly due to the electron donor density and electrical conductivity improvement.[20] The role of Si^{4+}, Sn^{4+}, and Ti^{4+} dopants in structural, electrical, and photoelectrochemical properties of hematite is then unclear; TAS analysis will be used to understand the change of optoelectronic and carrier dynamic characteristics in these doped materials.

The effect of co-catalyst loadings on SP-19 and SP-800 samples was also studied for improving its efficiency and photopotential. The SP-19 sample was coated with a thin layer of the NiFeOOH co-catalyst (SP-NiFeOOH) that allowed us to cathodically shift the onset potential to *ca*. 0.70 V_{RHE} and improved the overall PEC performance (see Figure 1d). NiFeOOH co-catalyst acts as a hole storage layer, avoiding holes to transfer back to the bulk of hematite and reducing the recombination at its surface.[15] On the other hand, SP-800 was further modified with IrO$_2$/RuO$_2$ co-catalysts (SP-800-IrO2RuO2), which improved mainly the low-bias performance: a low turn-on potential of *ca*. 0.50 V_{RHE} and an unprecedented photopotential of 1.20 V due to faster charge

transfer and reduced electron−hole recombination at its surface.[18] A photocurrent of *ca.* 1.26 mA·cm^{-2} was obtained at 1.45 V$_{RHE}$, corresponding to an *ca.* 40% increase compared to SP-800 without co-catalyst.

3.1.1. PEC Studies in the Presence of [Fe(CN)$_6$]$^{4-}$ Hole Scavenger. Further studies aimed at evaluating the performance of the prepared hematite photoelectrodes in NaOH electrolyte containing the Fe(CN)$_6^{4-}$ redox couple. Fe(CN)$_6^{4-}$ is a fast hole scavenger that deconvolutes the performance of the hematite films from the rate-limiting process of water oxidation; the photocurrent density is then strictly dependent on the fraction of photogenerated holes that reach the semiconductor−electrolyte interface.[17] Upon irradiation, electron−hole pair generation takes place in the hematite and holes move to its surface oxidizing Fe(CN)$_6^{4-}$ (ferrocyanide) to Fe(CN)$_6^{3-}$ (ferricyanide). Wedege et al.[6] reported the first aqueous alkaline solar redox flow cell (SRFC) using a ferrocyanide−hematite junction, where the photon energy is converted and stored directly as electrochemical energy, in the form of charged Fe(CN)$_6^{3-}$. The study of hematite performance in the presence of Fe(CN)$_6^{4-}$ hole scavenger is then very challenging to identify the bottlenecks preventing substantially higher efficiencies in SRFC. The role of hole scavengers, such as the Fe(CN)$_6^{4-/3-}$ and [IrCl$_6$]$^{4-/3-}$ redox pairs[17] and hydrogen peroxide,[25] was mainly studied to quantify the hole collection in PEC water splitting cells.

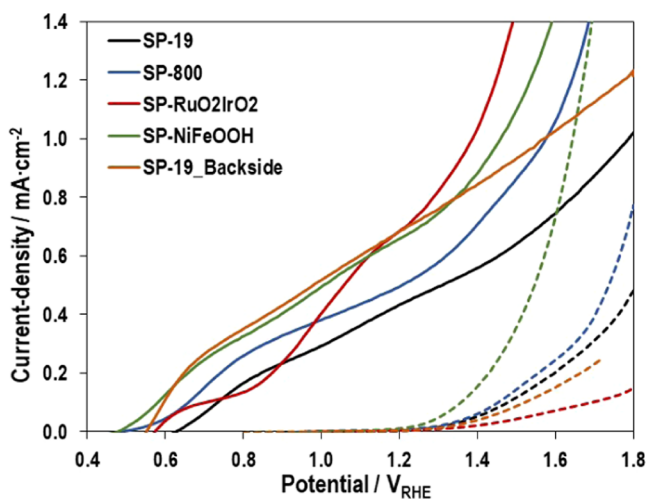Figure 2 shows the *J−V* curves of hematite photoelectrodes immersed in NaOH solution with the Fe(CN)$_6^{4-}$ redox pair

Figure 2. *J−V* characteristics of the hematite photoanodes immersed in 0.2 M K$_4$Fe(CN)$_6$ dissolved in 1 M NaOH, in the dark (dashed lines) and under 1-sun AM 1.5 G illumination (solid lines) conditions from the front side—100 mW·cm^{-2}; the reference SP-19 sample was also illuminated from the back side.

that revealed two different phenomena compared with only NaOH solution: (i) earlier onset potential and improved low-bias (potential up to 1.23 V$_{RHE}$) performance and (ii) photocurrent decrease for more than half at higher applied potentials; the SP-800-IrO$_2$RuO$_2$ sample was an exception. The SP-19 sample showed a shift on the onset potential from *ca.* 1.00 to 0.65 V$_{RHE}$, whereas for the SP-800 sample, the onset potential appeared at even more cathodic potentials, *ca.* 0.55 V$_{RHE}$, allowing an increase of the photopotential (800 mV). At high potentials, the observed photocurrent decrease is ascribed to the competitive light absorption by the hole scavenger, due

to the strong absorption of the Fe(CN)$_6^{4-}$ redox pair in the 300−400 nm range (see Figure S4 in the Supporting Information); under front-side illumination, the light passes first by the electrolyte film, being then absorbed by the hematite film side. Indeed, the hematite thin films also exhibit an absorption onset at ∼600 nm (2.06 eV, in agreement with the reported hematite bandgap values in the 2.0−2.2 eV range)[3] and wavelength maxima at ∼400 nm (Figure S4). Figure 2 shows the PEC behavior of the reference sample (SP-19) illuminated from the back-side illumination, *i.e.*, when the hematite photoelectrodes are illuminated through the FTO-glass substrate (no competitive light absorption occurs from the adjacent electrolyte), which revealed an improved performance for both the onset potential and photocurrent.

A cathodic shift of *ca.* 500 mV was obtained, which represents a gain of energy that must be understood for any practical use of hematite photoelectrodes in SRFCs. Klahr et al.[17] demonstrated that the photocurrent is strictly dependent on the amount of photogenerated holes that reach the semiconductor−electrolyte interface and is collected by the electrolyte redox species. This indicates that the water oxidation step is a rate-limiting step, which is more notable at lower potentials.[26] Due to slow hole transfer kinetics under water oxidation, the flux of holes that reach the hematite surface (that is just a property of the same bulk conditions) is the same in both the presence and absence of Fe(CN)$_6^{4-}$, but must either be trapped in surface states or recombine with electrons in the conduction band, whereas in the presence of a competitive hole scavenger, the photogenerated valence band holes at the hematite surface are efficiently collected by Fe(CN)$_6^{4-}$, and the charge transfer results in a steady-state photocurrent density at low-bias potentials. Preventing the recombination of bulk hematite electrons with long-lived holes accumulated at the semiconductor−electrolyte interface requires the application of stronger anodic bias (more positive potentials), and it is a key reason why the onset potential for photocurrent generation in hematite photoelectrodes is typically ∼500 mV anodic of the flat band. Despite this can be partially overcome with modification of the hematite surface, *e.g.*, depositing an efficient co-catalyst of IrO$_2$/RuO$_2$, as shown in Figure 1c, unexpected lower current values, even at more cathodic potentials, were observed when the sample SP-IrO$_2$RuO$_2$ was immersed in NaOH electrolyte with Fe-(CN)$_6^{4-}$—Figure 2. This behavior can be attributed to the efficient role of IrO$_2$/RuO$_2$ co-catalysts in decreasing the amount of photogenerated holes trapped in hematite surface states, due to enhanced charge transfer kinetics and then minimized back electron−hole recombination. On the other hand, the hematite performance improved after the deposition of the FeNiOOH co-catalyst in the presence of Fe(CN)$_6^{4-}$ redox pair, leading to a cathodic shift of *ca.* 300 mV (onset potential at *ca.* 0.50 V$_{RHE}$) compared with only NaOH solution, a photopotential of *ca.* 0.8 V, and a photocurrent density of *ca.* 0.51 mA·cm^{-2} at 1.00 V$_{RHE}$ (50% increase compared to bare hematite). These results demonstrated that different co-catalysts can play different roles, which are not always limited to changes in the surface properties but also to the bulk of the semiconductor. Understanding the effect of co-catalysts on the surface and bulk processes can provide new insights into the oxidation mechanism of water or a fast redox couple at hematite photoelectrodes.

3.1.2. Time-Resolved Transient Absorption Spectroscopy. To interpret the PEC behavior of the hematite photo-

electrodes, TAS measurements were carried out *in situ* or in operando. In general, TAS studies on hematite are performed as transmission experiments, where the information obtained is bulk-sensitive due to the penetration of the beam through the entire sample. Moreover, by conducting TAS measurements in the presence of the fast hole scavenger $Fe(CN)_6^{4-}$, it is expected to probe surface charge transfer reactions. Surface kinetics (at the semiconductor−liquid junction) competes with much faster charge recombination processes in the semiconductor bulk material.

Figure S4 presents the absorption spectra for the hematite photoelectrodes under study. No significant changes were found in the absorption onset between all of the analyzed samples, showing that this spectroscopic feature is not affected by the structural and morphological modifications introduced in the hematite films.

The present work started with the study of the TAS spectra and kinetics (in the femtosecond to microsecond time range) for the reference hematite planar thin film (SP-19 sample), Figure 3. These tests were performed using the cappuccino
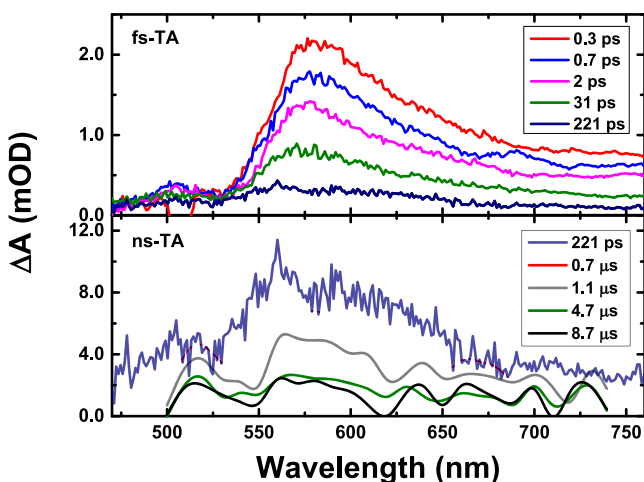

Figure 3. Transient absorption spectra obtained at different delay times, in the fs-TA and ns-TA apparatus, for the hematite SP-19 sample and collected under 1-sun illuminated irradiation applying a bias potential of *ca.* 1.40 V_{RHE}. For comparison, the spectra collected at 221 ps were normalized with the ns-TA data. The fs-TA data was collected with a pump pulse centered at 440 nm, while the ns-TA was obtained with excitation at 355 nm.

PEC cell in a three-electrode configuration (NaOH electrolyte) under 1-sun illumination and applying a constant bias potential of *ca.* 1.40 V_{RHE}. The long-term stability over 1000 h makes this hematite photoelectrode an excellent choice for TAS studies that require stable and reproducible measurements.[3]

Figure 3 shows a good agreement between the spectroscopic data obtained in the fs- and ns-TA apparatus, featuring both positive broad transient absorption bands in the range of 450−800 nm for the SP-19 sample. Similar TA spectra were obtained for the "dry" hematite films and immersed in electrolyte (1 M NaOH) with and without applied bias potential (see Figures S5−S7 in the Supporting Information). Previously, Pendlebury et al.[27] reported that the decay kinetics of photogenerated holes (monitored with 580 nm probe) in hematite films seem insensitive to the chemical environment, while Huang et al.[28] showed the negligible dependence of the

hematite TA features with the applied external bias, the solvent environment (*e.g.*, air, water, ethanol, methanol, and NaOH aqueous solutions), or the sample morphology (films of different thickness, nanoparticle films prepared by electrochemical deposition, and colloidal particle suspensions).

In agreement with previous reports, the transient absorption spectrum of hematite of the investigated hematite samples is characterized by a strong absorption band with maxima centered at *ca.* 580 nm and a tail that extends into the near-IR region.[2,28,29] Hematite charge carrier dynamics have been extensively investigated by TAS,[29,30] 4D electron energy loss spectroscopy,[31,32] and extreme ultraviolet spectroscopy.[33−35] The literature review reports relaxation dynamics in hematite, spanning a wide range of timescales and assigned them to processes such as charge carrier recombination, trapping, polaronic state formation, lattice expansion, and cooling of long-lived holes on the surface.[36] A detailed discussion of the transient behavior in hematite was recently reported by Forster et al.[30] and Miao et al.[35] Nevertheless, in a great number of past publications:[2,30,33,37,38] (i) for unbiased hematite samples or near to flat-band potential, *ca.* 0.5 V_{RHE}, the positive TA band centered at *ca.* 580 nm has been assigned to an electron trap state that lies a few hundred millielectronvolts below the conduction band edge, which will be partially occupied at the open circuit. While the TA band and kinetics for wavelengths >650 nm were assigned primarily to photoinduced absorption of hematite holes which under no applied bias potential exhibit rapid decay from subpicosecond to microsecond timescales; (ii) under anodic bias, *e.g.*, at 1.4 V_{RHE}, a similar initial broad positive photoinduced absorption was reported. However, it was shown that, contrary to flat-band conditions, under applied biases, these states become oxidized, enabling an optical transition to the localized trap states. However, the initial positive absorption maximum at *ca.* 580 nm rapidly inverts to a negative signal, which was assigned to photoelectron trapping (reduction) in the vacant states within the depletion layer. The recovery of this bleach signal was found to occur on the microsecond time scale and assigned, at least in part, to recombination of holes with these trapped electrons. For wavelengths >650 nm instead, anodic bias potential was found to retard the decay kinetics and therefore aid the generation of long-lived charge carriers.

Noteworthy is that for all hematite samples reported in this work (planar thin films and nanostructured samples) no bleaching of the 580 nm TA band was observed under 1.4 V_{RHE} anodic bias potential (see Figures 3 and S6 in the Supporting Information), thus suggesting that efficient electron injection from the hematite conduction band occurs, which significantly decreases the number of electron trap states. The low number of intraband electron trap states generated in these samples under anodic bias potential together with the strong overlap of photocarriers recombination signals can explain the absence of the 580 nm band bleaching in the pump-probe transient absorption difference spectra. The absence of the bleaching in the TA band centered at 580 nm supports the reduction of mid-gap electron trap states in the studied samples.

An alternative explanation for the positive 580 nm centered hematite band was given by Hayes et al.,[39] related to thermal effects arising from the laser-induced heating during a TA experiment that lead to lattice and thermal disorders, which dominate the TA spectrum of hematite and can be difficult to differentiate from excited-state absorptions. However, in the

Table 2. Transient Decay Lifetimes (τ_i) Obtained from the Global Fit Analysis to the TAS Data (*i.e.*, Simultaneous Analysis of the Decays Collected at 571, 610, and 700 nm) for the Hematite Photoelectrodes Varying the Film Thickness Obtained by fs- and ns-TA; Different Working Conditions Were Studied

samples	film thickness	τ_1 (ps)	τ_2 (ps)	τ_3 (ps)	τ_4 (μs)	τ_5 (μs)
SP-13	hematite film only—(i)	0.64	12	187		18
	(i) immersed in 1 M NaOH—(ii)	0.60	82	290	0.9	8
	(ii) + 1-sun and bias of 1.4 V$_{RHE}$—(iii)	0.82	14	160	0.5	10
SP-19	hematite film only—(i)	0.74	18	243		15
	(i) immersed in 1 M NaOH—(ii)	0.68	7	229	1.8	
	(ii) + 1-sun and bias of 1.4 V$_{RHE}$—(iii)	0.66	10	197	0.8	11
	(i) immersed in 1 M NaOH + K$_4$Fe(CN)$_6$—(iv)	0.97	33	289	1.8[a]	
	(iv) + 1-sun and bias of 1.4 V$_{RHE}$—(v)	1.1	24	272	0.8[a]	
SP-24	hematite film only—(i)				6.3	44
	(i) immersed in 1 M NaOH—(ii)	0.43	10	216	1.1	18
	(ii) + 1-sun and bias of 1.4 V$_{RHE}$—(iii)	0.57	10	193	0.8	5

[a]Lifetime fixed in the fs-TA analysis to the time obtained in the ns-TA setup under similar conditions.

Table 3. Transient Decay Lifetimes (τ_i) Obtained from the Global Fit Analysis to the TAS data (*i.e.*, Simultaneous Analysis of the Decays Collected at 571, 610, and 700 nm) for the Hematite Photoelectrodes with Different Morphologies (Samples Annealed at 800 °C) Obtained by fs- and ns-TA

samples	morphology	τ_1 (ps)	τ_2 (ps)	τ_3 (ps)	τ_4 (μs)	τ_5 (μs)
SP-800	hematite film only—(i)				49	806
	(i) immersed in 1 M NaOH—(ii)	0.88	24	244	3	27
	(ii) + 1-sun and bias of 1.4 V$_{RHE}$—(iii)	0.92	24	240	0.8	13
	(i) immersed in 1 M NaOH + K$_4$Fe(CN)$_6$—(iv)	0.82	33	323	0.8[a]	
	(iv) + 1-sun and bias of 1.4 V$_{RHE}$—(v)	0.83	33	344	0.8[a]	
NW-800	hematite film only—(i)				1.2	119
	(i) immersed in 1 M NaOH—(ii)	0.87	26	281	1.3	17
	(ii) + 1-sun and bias of 1.4 V$_{RHE}$—(iii)	0.91	24	265	1.1	13
	(i) immersed in 1 M NaOH + K$_4$Fe(CN)$_6$—(iv)	0.74	19	226	1.3[a]	
	(iv) + 1-sun and bias of 1.4 V$_{RHE}$—(v)	1	37	284	1.1[a]	

[a]Lifetime fixed in the fs-TA analysis to the time obtained in the ns-TA setup under similar conditions.

Table 4. Transient Decay Lifetimes (τ_i) Obtained from the Global Fit Analysis to the TAS data (*i.e.*, Simultaneous Analysis of the Decays Collected at 571, 610, and 700 nm) for the Sn-, Si-, and Ti-Doped Hematite Photoelectrodes Obtained by fs- and ns-TA

samples	doping	τ_1 (ps)	τ_2 (ps)	τ_3 (ps)	τ_4 (μs)	τ_5 (μs)
SP-800	sample intrinsically doped with Sn; see data in Table 3					
SP-Si	hematite film only—(i)	0.84	19	258	9	91
	(i) immersed in 1 M NaOH—(ii)	1.6	21	400	1.3	29
	(ii) + 1-sun and bias of 1.4 V$_{RHE}$—(iii)	0.74	12	259	0.9	13
	(i) immersed in 1 M NaOH + K$_4$Fe(CN)$_6$—(iv)	0.51	6	217	1.3[a]	
	(iv) + 1-sun and bias of 1.4 V$_{RHE}$—(v)	0.45	8	293	0.9[a]	
NW-Ti	hematite film only—(i)				7	403
	(i) immersed in 1 M NaOH—(ii)	0.82	22	311	2.1	88
	(ii) + 1-sun and bias of 1.4 V$_{RHE}$—(iii)	0.91	20	374	2.4	72

[a]Lifetimes fixed in the fs-TA analysis to the time obtained in the ns-TA setup under similar conditions.

present work, the TAS studies were carried out with low laser excitation energies, which in principle avoided the formation of high photoinduced charge carrier densities (and therefore fast bimolecular (nongeminate) recombination) and sample thermal heating. Indeed, previous ultrafast studies for hematite have reported almost complete recombination within a few hundred picoseconds and attributed to the relatively high carrier densities sometimes generated in ultrafast spectroscopy, which can accelerate recombination rates.[37] Thus, we assign the TA signal centered at 580 nm in Figure 3 to the absorption of photoexcited holes. Indeed, it has been shown that the TA fingerprints of photoexcited holes are frequently reported to appear at 500−600 nm on different semiconductors, while the TA signatures of photoexcited electrons typically occur in the NIR region.[35]

3.1.3. TAS Kinetic Analysis. Global fit analysis was performed with singular-value decomposition to better describe the observed ultrafast TAS dynamics. In this analysis, the kinetic traces (at different wavelengths) are fitted with the same (multi)exponential equation and lifetimes bound for all wavelengths, while their amplitudes are free to vary. This type of analysis is useful for extracting kinetic information of the TAS data, since different types of charge carriers can contribute to the TA signal at different probe wavelengths.[35]

Table 5. Transient Decay Lifetimes (τ_i) Obtained from the Global Fit Analysis to the TAS data (*i.e.*, Simultaneous Analysis of the Decays Collected at 571, 610, and 700 nm) for the Hematite Photoelectrodes with Surface Treatment with Different Co-Catalysts (Surface Passivation) Obtained by fs- and ns-TA

samples	surface passivation with co-catalysts	τ_1 (ps)	τ_2 (ps)	τ_3 (ps)	τ_4 (μs)	τ_5 (μs)
SP-800-IrO$_2$RuO$_2$	hematite film only—(i)	0.94	41	368	14	132
	(i) immersed in 1 M NaOH—(ii)		2.8	231	1.1	16
	(ii) + 1-sun and bias of 1.4 V$_{RHE}$—(iii)	0.85	34	332	0.8	16
	(i) immersed in 1 M NaOH + K$_4$Fe(CN)$_6$—(iv)	0.69	19	230	1.1[a]	
	(iv) + 1-sun and bias of 1.4 V$_{RHE}$—(v)	0.71	12	202	0.8[a]	
SP-NiFeOOH	hematite film only—(i)				9	168
	(i) immersed in 1 M NaOH—(ii)	0.87	24	259	0.6	32
	(ii) + 1-sun and bias of 1.4 V$_{RHE}$—(iii)	0.78	17	233	1.1	11
	(i) immersed in 1 M NaOH + K$_4$Fe(CN)$_6$—(iv)	0.74	19	226	0.6[a]	
	(iv) + 1-sun and bias of 1.4 V$_{RHE}$—(v)	1.0	37	285	1.1[a]	

[a]Lifetimes fixed in the fs-TA analysis to the time obtained in the ns-TA setup under similar conditions.

Therefore, certain kinetic components can be expected to be common across different wavelengths. Tables 2−5 present the obtained results of the best fits to the transient absorption data for the hematite samples under study, in which τ_1, τ_2, and τ_3 transient decay lifetimes result from the fs-TA data and τ_4 and τ_5 result from ns-TA data. In general, the ns-TA decays were well fitted with a double-exponential decay law, whereas the analysis of the fs-TA data was performed by global fit analysis of all of the kinetics in the 530−740 nm range, taking into account the transient lifetimes in the ns-TA data (*i.e.*, fixing the long decay time in the analysis to the value obtained by ns-TA data). This procedure was necessary to ensure the best fit to the transient absorption data in the femtosecond to microsecond time range (see Figures S8 and S9 in the Supporting Information with the best fits to the representative kinetic traces obtained for the SP-19 sample). The working conditions tested (presented in Tables 2−5) were the following: (i) the dry isolated film (hematite film only); (ii) the hematite sample (i) immersed in 1 M NaOH electrolyte, in the dark and without applied bias potential; (iii) a three-electrode configuration, where the hematite sample is immersed in 1 M NaOH electrolyte—condition (ii), under 1-sun illumination (100 mW·cm^{-2}) and applying a bias potential of *ca.* 1.4 V$_{RHE}$; (iv) the hematite sample (i) immersed in 10 mM K$_4$Fe(CN)$_6$ dissolved in 1 M NaOH electrolyte, in the dark and without applied bias potential; and (v) a three-electrode configuration, where the hematite sample is immersed in 10 mM K$_4$Fe(CN)$_6$ dissolved in 1 M NaOH electrolyte solution—condition (iv), under 1-sun illumination and applying a bias potential of *ca.* 1.4 V$_{RHE}$.

In general, the TA data of the studied hematite samples (see Tables 2−5) present: (i) a first fast decay transient, τ_1, with values ranging from 0.43 to 1.6 ps; (ii) a second one, τ_2, with values in the 2.8−41 ps range; (iii) a third one, τ_3, with values ranging from 160 to 400 ps; (iv) in the microsecond time range, transient lifetimes in the 0.5−49 μs range, τ_4; and (v) long-lived transients ranging from 5 to 806 μs, τ_5. These lifetimes are in good agreement with the values reported for 50 nm thick hematite photoelectrodes made by atomic layer deposition (TAS data obtained in air),[40] in which: (i) the fast τ_1 transient lifetime was assigned to the initial relaxation of hot electrons; (ii) the τ_2 and τ_3 values to recombination of free conduction electrons trapped by mid-gap states; and (iii) the τ_4 to τ_5 lifetimes to the slower recombination dynamics of the remaining free and mid-gap trapped electrons.[29]

It is worth mentioning that from Tables 2−5, it can be seen that, going from the dry hematite thin films to the samples immersed in 1 M NaOH and applying an anodic bias potential, a significant decrease of the longest lifetimes (mainly in τ_3 and in the microsecond range lifetimes, τ_4 and τ_5) is observed, thus showing that contrary to what was expected, the charge recombination of trapped holes and electrons is faster in operando conditions. Indeed, applied anodic bias has been recognized as a way to retard ultrafast recombination in the bulk hematite.[37]

Taking the hematite planar thin film with *ca.* 19 nm (SP-19) as the reference sample, the influence of several parameters on the charge carrier dynamics was studied evaluating the transient absorption lifetimes: (1) the thickness of the hematite planar film; (2) the role of morphology (surface smoothening by high-temperature annealing and nanostructuring); (3) *ex situ* doping (3% Si on planar films and Ti-doped nanostructures); and (4) surface treatments (co-catalyst coatings, such as IrO$_2$/RuO$_2$ and NiFeOOH). Two conditions were also considered, namely, the dry film (standalone hematite samples as working electrodes) and the hematite sample immersed in 1 M NaOH (supporting electrolyte), in the dark and without bias potential. In general, similar positive broad transient absorption bands to those found for the SP-19 sample (Figure 3a, fs-TA) were observed for all hematite films, with maxima at 575−580 nm (see Figures S5 and S6 in the Supporting Information).

In this work, two electron−hole recombination timescales will be discussed: (i) the fast charge recombination in the subnanosecond ascribed to free conduction mid-gap electron−hole recombination, *i.e.*, the majority charge carriers formed upon photoexcitation (τ_2 and τ_3 lifetimes that in the fs-TA decays present the higher associated preexponential factors, *i.e.*, the two major contributions for the total decay; see Tables S2−S5 in the Supporting Information) and responsible for the efficiency losses in PEC applications; and (ii) the microsecond lifetimes (τ_4 and τ_5) assigned to the lower recombination of trapped electrons and holes (minority charge carriers).

3.1.3.1. Film Thickness. Table 2 presents the TAS data for the hematite photoanodes with film thickness varying from 13 to 24 nm (samples SP-13 and SP-24, respectively). Although the samples with the 19 nm (SP-19) showed the best photocurrent density at all applied potentials (Figure 1), no significant differences were found among different thicknesses in the TA lifetimes and associated preexponential values (see Tables S2−S5 in the Supporting Information). However,

compared with the 50 nm thick ALD-deposited hematite films elsewhere reported, the lifetimes associated with charge carrier recombination, τ_{2-5}, are considerably higher for the hematite photoanodes under investigation (*e.g.*, 1.6 *vs* 18 ps, 46 *vs* 243 ps, and 2.4 ns *vs* 15 μs, for the 50 nm ALD film and SP-19 in air, respectively; see Table 2).[40] Indeed, the poor carrier mobilities and short hole diffusion lengths in hematite[2] promotes the fast electron−hole recombination in the bulk of thick films, which hinders the PEC application of thick planar hematite films.

3.1.3.2. Morphology. Table 3 presents the TAS data for the planar hematite thin film with *ca.* 19 nm and the nanowired hematite film with *ca.* 500 nm prepared by hydrothermal treatment, both annealed at 800 °C, samples SP-800 and NW-800, respectively. High-temperature annealing treatment at 800 °C was found to enhance the hematite crystallinity and decrease the recombination surface states, leading to higher bulk conductivity.[38,41,42]

Analyzing Tables 2 and 3, a significant increase in the recombination lifetime is observed associated with the minority charge carriers τ_5, going from the bare hematite SP-19 sample to the annealed film SP-800 sample (15 *vs* 806 μs, respectively), when the TAS is collected for the film only. From the comparison of the SP-19 and SP-800 samples in operando (1-sun and bias of 1.4 V_{RHE}), no significant changes were found in the microsecond time scale. However, the lifetimes associated with the majority carriers, τ_2 and τ_3, increase with the high-temperature treatment (10 *vs* 33 ps and 197 *vs* 240 ps, respectively).

When comparing the planar and nanowired hematite samples (Table 3), no significant differences were found in the kinetic data in TAS obtained in operando, thus showing that the higher surface area of the NW-800 sample does not influence the charge recombination dynamics. Therefore, the effect of the morphological change on the electron dynamics in hematite is negligible on the subnanosecond time scale.

3.1.3.3. Doping. Hematite is typically doped for increasing the charge carrier concentration, therefore improving the PEC performance.[36] However, it is difficult to tell what is the best dopant as well as what are the reasons for improving the performance of hematite photoanodes.

The transient absorption data for the Si- and Sn-doped planar thin hematite photoelectrodes (SP-Si and SP-800 samples, respectively) and for the Ti-doped nanostructured hematite photoelectrodes (NW-Ti sample) are shown in Tables 3 and 4. In operando conditions (under 1-sun illumination and a bias potential of 1.40 V_{RHE}), similar spectroscopic features ($\lambda_{máx} \sim 585$ nm) and transient decay kinetics were found for both doped planar thin films, whereas for the NW-Ti sample, slower recombination lifetimes were observed for the transient lifetimes τ_3 and τ_5. Moreover, the time-resolved ns-TA data for the NW-Ti photoelectrode in operando shows that the band centered at 585 nm disappears and a new band arises with a maximum at *ca.* 550 nm (at higher delay times; see Figure 4B), whereas when no potential is applied, an increase in absorption intensity of the 585 nm TA band together with a redshift of the maxima of the shortest-wavelength transient absorption band of *ca.* 10 nm was observed compared with the data in operando (Figure 4). Barroso et al.[2] reported a similar behavior for the Si-doped nanostructured hematite photoelectrodes, *i.e.*, the TA characteristic hematite band centered at 580 nm disappears with the increase of the applied bias potential due to fast trap-mediated
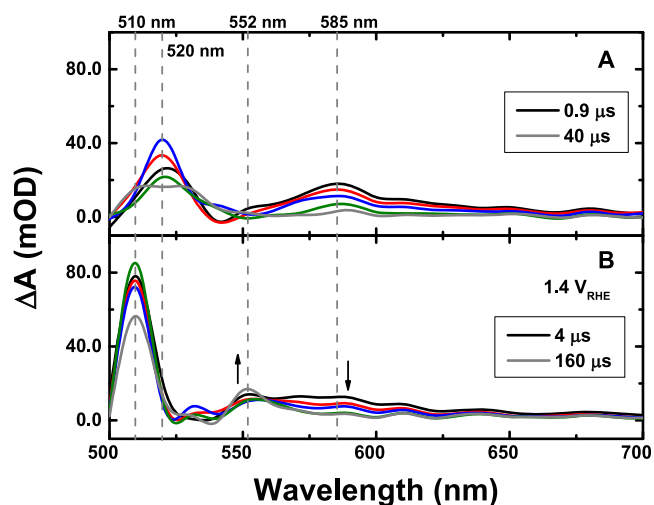

Figure 4. Time-resolved transient absorption spectra obtained with laser excitation at 355 nm for the NW-Ti sample collected in (A) 1 M NaOH solution and (B) in a three-electrode configuration applying a bias potential of 1.40 V_{RHE} and under 1-sun illumination.

electron−hole recombination. In addition, in that case, two distinctive spectral trends were identified: (i) the appearance of a broad, long-lived transient absorption band (from 550 to 900 nm, with a maximum at 650 nm); and (ii) a relatively narrow, negative transient absorption (bleach) band centered at 580 nm, which corresponds to a reduction of the intraband states located below the conduction band and within the space charge layer, *i.e.*, to electron trapping, resulting from the photoexcitation in the space charge layer. As such, these trapped electrons may either recombine with holes within the bulk or be extracted of the space charge layer by the electric field and then be collected in the external circuit.[2] However, since in the present study no significant decay of the positive 650 nm transient absorption signal was detected for the NW-Ti sample, the observed photocurrent enhancement with a stepwise shape after 1.0 V_{RHE} can be attributed to the reduced electron−hole recombination within the space charge region of the hematite and also to the expected increase of electron density.[32] This can be also justified by the later onset potential (shifted *ca.* 100 mV to more anodic potentials) in comparison to the Sn-doped hematite thin films (SP-800 sample). In fact, the Sn doping promoted by the thermally induced diffusion of Sn ions from the FTO layer in a thin film may enhance the electron donor density and suppress the amount of surface states.[18] The negligible effect on the charge carrier dynamics on the picosecond time scale going from the bare hematite film (SP-19) to the Sn-doped, SP-800, together with what was previously reported for Sn-doped nanostructured hematite photoanodes,[43] may support this conclusion. Indeed, previous ultrafast TAS studies of Sn-doped nanostructured hematite showed that, in agreement with our data (see Table 4), the overall charge carrier decays for hematite nanowires are very fast, with transient lifetimes of 0.35, 2.3, and 67.4 ps for the samples annealed at 800 °C.[43] The very fast decays were associated with the high density of band gap electronic states caused by internal defects and/or surface defects, and it was concluded that the Sn doping percentage increase cannot reduce the rapid loss of photoexcited electron through very fast charge recombination. On the other hand, the Si-doped thin film showed a higher photocurrent than the Ti-doped

nanostructured film for potentials above 1.40 V_{RHE} (compared with the SP-800 sample, it is higher after 1.20 V_{RHE}), showing that the Si incorporation may efficiently enhance the hopping probably of charge carriers to the hematite surface, since at these potentials, the photocurrent density is controlled by the number of holes that reach its surface to participate in the water oxidation reaction. Although this was not proved by the TAS analysis on the time scale studied, significant changes in carrier lifetimes may occur on microsecond to millisecond scales.

It is important to refer that these observations were not always consistent with other reports on doped hematite photoelectrodes, suggesting that the photoelectrochemical and electronic properties depend not only on the dopant identity and its concentration but also on the distribution and the film morphology in which the dopant is incorporated.

3.1.3.4. Surface Passivation with Co-Catalysts. In this work, two co-catalysts (thin dual layer of IrO_2 and RuO_2, SP-800-IrO_2RuO_2 sample, and thin layer of NiFeOOH, SP-NiFeOOH sample) were deposited on top of hematite planar photoelectrodes to reduce hole trapping and enhance oxidation reaction kinetics. The TAS data for these hematite photoelectrodes are presented in Table 5; the SP-800-IrO_2RuO_2 sample can be compared with the SP-800 sample (see Table 3), while the SP-NiFeOOH sample would be compared with the SP-19 sample (see Table 2). According to absorption spectra analysis (Figure S4 in the Supporting Information), the IrO_2/RuO_2 co-catalyst does not present a significant contribution for light harvesting. Therefore, it is assumed that the electrons and holes were only generated from the hematite photoelectrode. The deposition of an overlayer can partly or entirely cover the defects of the outermost hematite, thus reducing surface Fe^{2+}–V_O recombination and other possible types of surface states.[38]

The comparison between Tables 3 and 5 shows that in operando conditions, the recombination lifetimes, τ_2 and τ_3, increased with the IrO_2/RuO_2 co-catalysts coating, 24 *vs* 34 ps and 240 *vs* 332 ps, respectively for SP-800 and SP-800-IrO_2RuO_2 samples, while in the microsecond time scale, no significant changes were observed in the slower charge recombination lifetimes. When comparing SP-19 and SP-NiFeOOH samples (Tables 2 and 5, respectively), no significant changes in the transient lifetimes were observed for the different hematite photoelectrodes in the subnanosecond and microsecond ranges. These results contradict the ones reported in the literature for hematite with an amorphous co-catalyst of NiFeO$_x$[44,45] which showed that the intensity of components in the microseconds to seconds time region, arising from trapped electrons and holes at surface states, was increased after catalyst deposition due to the improvement of the charge separation efficiency.

It is noteworthy that although in this work one of the best PEC performances for planar thin films were obtained for the SP-NiFeOOH photoelectrode, the TAS kinetic data did not display considerable changes in the recombination rate constants that could be correlated to the improved PEC properties (*i.e.*, higher efficiency in charge carrier collection). Indeed, it is known that slower recombination dynamics and/ or with lower recombination losses/sites (or associated kinetics) strongly contributes to better performances. However, in agreement with the overall data collected for this sample, the TA data also demonstrate that the majority of the charge carrier recombination occurs in the subnanosecond

time scale (as shown by the high preexponential values associated with the electron–hole recombination τ_2 and τ_3 in Table S4).

3.1.4. TAS Studies of the Hematite Films in the Presence of the FeCN$_6^{4-}$ Redox Pair. The transient lifetimes of the charge carriers in the hematite photoelectrodes were also studied in a solar redox flow cell loaded with $Fe(CN)_6^{4-}$ redox pair (known as a fast hole scavenger). The absorption spectra of 10 mM $K_4Fe(CN)_6$ diluted in 1 M NaOH presents an absorption onset at *ca.* 400 nm (Figure S4); after laser excitation at 355 nm, a broad transient absorption spectrum in the 320–700 nm range was found, as seen in Figure S10A. For this reason, attempts were made to measure the nanosecond to microsecond transient absorption (in the ns-TA setup, with excitation wavelengths limited to the harmonics of the Nd:YAG laser, 532, 355, and 266 nm) of the hematite samples (absorption band onset ~600 nm) with excitation at 532 nm (in a region where the $Fe(CN)_6^{4-}$ redox pair does not absorb). However, the TA signal characteristic of hematite was unable to be observed, which was attributed to the low absorbance and absorption cross section of the studied hematite films at 532 nm (Figure S4). However, it was possible to obtain the TAS for all of the hematite samples in the presence of $Fe(CN)_6^{4-}$ redox pair (dissolved in 1 M NaOH) using the fs-TA setup with 440 nm excitation (in a region where the pump light is not absorbed by the hole scavenger, Figure S4). Similar methodology and experimental protocols were followed, namely, a three-electrode configuration with and without an applied bias potential of 1.40 V_{RHE}. The results from the best fit to the transient kinetic data are presented in Tables 2–5. The results show that within experimental error, the fast transient lifetimes τ_2–τ_3 (associated with free conduction mid-gap electron–hole recombination) are not affected by the presence of the hole scavenger. Therefore, the recombination lifetimes determined by TAS studies on these timescales can be attributed mainly to charge carriers generated in the bulk of the hematite films, which reinforces the previous conclusions.

4. CONCLUSIONS

The performance of hematite photoelectrodes was studied varying the film morphology (planar and nanostructured), the thickness of planar thin films, the addition of dopants, and the surface treatments (high-temperature annealing and co-catalyst loading). A hematite thin film annealed at 800 °C (intrinsically Sn-doped) and activated with RuO_2/IrO_2 co-catalyst displayed the lowest onset potential (*ca.* 0.52 V_{RHE}) and the highest photocurrent at 1.45 V_{RHE} (*ca.* 1.26 mA·cm^{-2}). However, Ti-doped nanowired photoelectrode showed the best fill factor, *i.e.*, it showed a stepwise shape at *ca.* 1.0 V_{RHE} with photocurrents higher than 1 mA·cm^{-2} after 1.1 V_{RHE}; thus, an enhancement in PEC performance is expected when a co-catalyst is deposited. From the TAS study, it was concluded that the charge carrier recombination dynamics occurs in the bulk of the hematite films with subnanosecond lifetimes and the charge carrier dynamics do not present a significant correlation with the PEC efficiency. Only a slower electron–hole recombination at the hematite space charge region and increased charge carrier density for the Ti-doped nanowires related to the Ti incorporation and enlarged surface area were observed. The best performance was obtained for the planar thin film intrinsically doped with Sn and coated with RuO_2/IrO_2 co-catalyst, which was attributed to the improved donor density and electrical conductivity. Concerning the presence of

the fast redox couple of $FeCN_6^{4-}$, the fast transient lifetimes associated with the recombination phenomena are not affected, thus corroborating that the subnanosecond recombination lifetimes are mainly from charge carriers generated in the bulk of the hematite films.

■ ASSOCIATED CONTENT

Ⓢ Supporting Information

The Supporting Information is available free of charge at https://pubs.acs.org/doi/10.1021/acs.jpcc.0c11420.

> Hematite planar films and nanowires (NW) and preparation methods; $J-V$ characteristics of undoped hematite NWs; absorption spectra; time-resolved transient absorption data; and transient decay lifetimes and associated preexponential values (PDF)

■ AUTHOR INFORMATION

Corresponding Authors

   João Pina − *Coimbra Chemistry Centre, Department of Chemistry, University of Coimbra, 3004-535 Coimbra, Portugal;* ⓘ orcid.org/0000-0003-1848-1167; Email: jpina@qui.uc.pt

   Paula Dias − *LEPABE—Laboratory for Process Engineering, Environment, Biotechnology and Energy, Faculty of Engineering, University of Porto, 4200-465 Porto, Portugal;* ⓘ orcid.org/0000-0002-3837-0715; Email: pauladias@fe.up.pt

Authors

   Carlos Serpa − *Coimbra Chemistry Centre, Department of Chemistry, University of Coimbra, 3004-535 Coimbra, Portugal;* ⓘ orcid.org/0000-0001-7004-0110

   João Azevedo − *LEPABE—Laboratory for Process Engineering, Environment, Biotechnology and Energy, Faculty of Engineering, University of Porto, 4200-465 Porto, Portugal*

   Adélio Mendes − *LEPABE—Laboratory for Process Engineering, Environment, Biotechnology and Energy, Faculty of Engineering, University of Porto, 4200-465 Porto, Portugal;* ⓘ orcid.org/0000-0003-2472-3265

   João Sérgio Seixas de Melo − *Coimbra Chemistry Centre, Department of Chemistry, University of Coimbra, 3004-535 Coimbra, Portugal;* ⓘ orcid.org/0000-0001-9708-5079

Complete contact information is available at:
https://pubs.acs.org/10.1021/acs.jpcc.0c11420

Notes

The authors declare no competing financial interest.

■ ACKNOWLEDGMENTS

■ REFERENCES

(1) Lopes, T.; Andrade, L.; Le Formal, F.; Gratzel, M.; Sivula, K.; Mendes, A. Hematite photoelectrodes for water splitting: evaluation of the role of film thickness by impedance spectroscopy. *Phys. Chem. Chem. Phys.* **2014**, *16*, 16515−16523.

(2) Barroso, M.; Pendlebury, S. R.; Cowan, A. J.; Durrant, J. R. Charge carrier trapping, recombination and transfer in hematite (α-Fe2O3) water splitting photoanodes. *Chem. Sci.* **2013**, *4*, 2724−2734.

(3) Dias, P.; Vilanova, A.; Lopes, T.; Andrade, L.; Mendes, A. Extremely stable bare hematite photoanode for solar water splitting. *Nano Energy* **2016**, *23*, 70−79.

(4) Azevedo, J.; Seipp, T.; Burfeind, J.; Sousa, C.; Bentien, A.; Araújo, J. P.; Mendes, A. Unbiased solar energy storage: Photoelectrochemical redox flow battery. *Nano Energy* **2016**, *22*, 396−405.

(5) Khataee, A.; Azevedo, J.; Dias, P.; Ivanou, D.; Dražević, E.; Bentien, A.; Mendes, A. Integrated design of hematite and dye-sensitized solar cell for unbiased solar charging of an organic-inorganic redox flow battery. *Nano Energy* **2019**, *62*, 832−843.

(6) Wedege, K.; Azevedo, J.; Khataee, A.; Bentien, A.; Mendes, A. Direct Solar Charging of an Organic−Inorganic, Stable, and Aqueous Alkaline Redox Flow Battery with a Hematite Photoanode. *Angew. Chem., Int. Ed.* **2016**, *55*, 7142−7147.

(7) Sivula, K. Nanostructured Fe$_2$O$_3$ Photoanodes. In *Electronic Materials: Science & Technology*, van de Krol, R.; Grätzel, M., Eds.; Springer: US, 2012; Vol. 102, pp 121−156.

(8) Klotz, D.; Ellis, D. S.; Dotan, H.; Rothschild, A. Empirical in operando analysis of the charge carrier dynamics in hematite photoanodes by PEIS, IMPS and IMVS. *Phys. Chem. Chem. Phys.* **2016**, *18*, 23438−23457.

(9) Tang, P.; Arbiol, J. Engineering surface states of hematite based photoanodes for boosting photoelectrochemical water splitting. *Nanoscale Horiz.* **2019**, *4*, 1256−1276.

(10) Wheeler, D. A.; Wang, G.; Ling, Y.; Li, Y.; Zhang, J. Z. Nanostructured hematite: synthesis, characterization, charge carrier dynamics, and photoelectrochemical properties. *Energy Environ. Sci.* **2012**, *5*, 6682−6702.

(11) Pei, G. X.; Wijten, J. H. J.; Weckhuysen, B. M. Probing the dynamics of photogenerated holes in doped hematite photoanodes for solar water splitting using transient absorption spectroscopy. *Phys. Chem. Chem. Phys.* **2018**, *20*, 9806−9811.

(12) Barroso, M.; Mesa, C. A.; Pendlebury, S. R.; Cowan, A. J.; Hisatomi, T.; Sivula, K.; Grätzel, M.; Klug, D. R.; Durrant, J. R. Dynamics of photogenerated holes in surface modified α-Fe$_2$O$_3$ photoanodes for solar water splitting. *Proc. Natl. Acad. Sci. U.S.A.* **2012**, *109*, 15640−15645.

(13) Vayssieres, L.; Beermann, N.; Lindquist, S.-E.; Hagfeldt, A. Controlled Aqueous Chemical Growth of Oriented Three-Dimen-

sional Crystalline Nanorod Arrays: Application to Iron(III) Oxides. *Chem. Mater.* **2001**, *13*, 233−235.

(14) Lopes, T.; Andrade, L.; Ribeiro, H. A.; Mendes, A. Characterization of photoelectrochemical cells for water splitting by electrochemical impedance spectroscopy. *Int. J. Hydrogen Energy* **2010**, *35*, 11601−11608.

(15) Pina, J.; Queiroz, M. J. R. P.; Seixas de Melo, J. Effect of substitution on the ultrafast deactivation of the excited state of benzo[b]thiophene-arylamines. *Photochem. Photobiol. Sci.* **2016**, *15*, 1029−1038.

(16) Pina, J.; Burrows, H. D.; Becker, R. S.; Dias, F. B.; Maçanita, A. L.; Seixas de Melo, J. Photophysical Studies of alpha,w -Dicyano-oligothiophenes NC(C4H2S)nCN (n = 1−6). *J. Phys. Chem. B* **2006**, *110*, 6499−6505.

(17) Klahr, B. M.; Hamann, T. W. Current and Voltage Limiting Processes in Thin Film Hematite Electrodes. *J. Phys. Chem. C* **2011**, *115*, 8393−8399.

(18) Dias, P.; Andrade, L.; Mendes, A. Hematite-based photo-electrode for solar water splitting with very high photovoltage. *Nano Energy* **2017**, *38*, 218−231.

(19) Subramanian, A.; Gracia-Espino, E.; Annamalai, A.; Lee, H. H.; Lee, S. Y.; Choi, S. H.; Jang, J. S. Effect of tetravalent dopants on hematite nanostructure for enhanced photoelectrochemical water splitting. *Appl. Surf. Sci.* **2018**, *427*, 1203−1212.

(20) Chemelewski, W. D.; Hahn, N. T.; Mullins, C. B. Effect of Si Doping and Porosity on Hematite's (α-Fe$_2$O$_3$) Photoelectrochemical Water Oxidation Performance. *J. Phys. Chem. C* **2012**, *116*, 5255−5261.

(21) Wang, Q.; Chen, Y.; Xu, J.; Situ, Y.; Huang, H. Morphology-controlled synthesis of Ti-doped α-Fe2O3 nanorod arrays as an efficient photoanode for photoelectrochemical applications. *Res. Chem. Intermed.* **2018**, *44*, 2365−2378.

(22) Li, M.; Yang, Y.; Ling, Y.; Qiu, W.; Wang, F.; Liu, T.; Song, Y.; Liu, X.; Fang, P.; Tong, Y.; Li, Y. Morphology and Doping Engineering of Sn-Doped Hematite Nanowire Photoanodes. *Nano Lett.* **2017**, *17*, 2490−2495.

(23) Li, S.; Cai, J.; Liu, Y.; Gao, M.; Cao, F.; Qin, G. Tuning orientation of doped hematite photoanodes for enhanced photo-electrochemical water oxidation. *Sol. Energy Mater. Sol. Cells* **2018**, *179*, 328−333.

(24) Tamirat, A. G.; Rick, J.; Dubale, A. A.; Su, W.-N.; Hwang, B.-J. Using hematite for photoelectrochemical water splitting: a review of current progress and challenges. *Nanoscale Horiz.* **2016**, *1*, 243−267.

(25) Dotan, H.; Sivula, K.; Grätzel, M.; Rothschild, A.; Warren, S. C. Probing the photoelectrochemical properties of hematite (α-Fe$_2$O$_3$) electrodes using hydrogen peroxide as a hole scavenger. *Energy Environ. Sci.* **2011**, *4*, 958−964.

(26) Le Formal, F.; Pendlebury, S. R.; Cornuz, M.; Tilley, S. D.; Grätzel, M.; Durrant, J. R. Back Electron−Hole Recombination in Hematite Photoanodes for Water Splitting. *J. Am. Chem. Soc.* **2014**, *136*, 2564−2574.

(27) Pendlebury, S. R.; Barroso, M.; Cowan, A. J.; Sivula, K.; Tang, J.; Grätzel, M.; Klug, D.; Durrant, J. R. Dynamics of photogenerated holes in nanocrystalline α-Fe$_2$O$_3$ electrodes for water oxidation probed by transient absorption spectroscopy. *Chem. Commun.* **2011**, *47*, 716−718.

(28) Huang, Z.; Lin, Y.; Xiang, X.; Rodríguez-Córdoba, W.; McDonald, K. J.; Hagen, K. S.; Choi, K.-S.; Brunschwig, B. S.; Musaev, D. G.; Hill, C. L.; Wang, D.; Lian, T. In situ probe of photocarrier dynamics in water-splitting hematite (α-Fe$_2$O$_3$) electrodes. *Energy Environ. Sci.* **2012**, *5*, 8923−8926.

(29) Sorenson, S.; Driscoll, E.; Haghighat, S.; Dawlaty, J. M. Ultrafast Carrier Dynamics in Hematite Films: The Role of Photoexcited Electrons in the Transient Optical Response. *J. Phys. Chem. C* **2014**, *118*, 23621−23626.

(30) Forster, M.; Cheung, D. W. F.; Gardner, A. M.; Cowan, A. J. Potential and pitfalls: On the use of transient absorption spectroscopy for in situ and operando studies of photoelectrodes. *J. Chem. Phys.* **2020**, *153*, No. 150901.

(31) Su, Z.; Baskin, J. S.; Zhou, W.; Thomas, J. M.; Zewail, A. H. Ultrafast Elemental and Oxidation-State Mapping of Hematite by 4D Electron Microscopy. *J. Am. Chem. Soc.* **2017**, *139*, 4916−4922.

(32) Yang, T.-Y.; Kang, H.-Y.; Jin, K.; Park, S.; Lee, J.-H.; Sim, U.; Jeong, H.-Y.; Joo, Y.-C.; Nam, K. T. An iron oxide photoanode with hierarchical nanostructure for efficient water oxidation. *J. Mater. Chem. A* **2014**, *2*, 2297−2305.

(33) Biswas, S.; Husek, J.; Londo, S.; Baker, L. R. Highly Localized Charge Transfer Excitons in Metal Oxide Semiconductors. *Nano Lett.* **2018**, *18*, 1228−1233.

(34) Carneiro, L. M.; Cushing, S. K.; Liu, C.; Su, Y.; Yang, P.; Alivisatos, A. P.; Leone, S. R. Excitation-wavelength-dependent small polaron trapping of photoexcited carriers in α-Fe$_2$O$_3$. *Nat. Mater.* **2017**, *16*, 819−825.

(35) Miao, T. J.; Tang, J. Characterization of charge carrier behavior in photocatalysis using transient absorption spectroscopy. *J. Chem. Phys.* **2020**, *152*, No. 194201.

(36) Kay, A.; Fiegenbaum-Raz, M.; Müller, S.; Eichberger, R.; Dotan, H.; van de Krol, R.; Abdi, F. F.; Rothschild, A.; Friedrich, D.; Grave, D. A. Effect of Doping and Excitation Wavelength on Charge Carrier Dynamics in Hematite by Time-Resolved Microwave and Terahertz Photoconductivity. *Adv. Funct. Mater.* **2020**, *30*, No. 1901590.

(37) Pendlebury, S. R.; Wang, X.; Le Formal, F.; Cornuz, M.; Kafizas, A.; Tilley, S. D.; Grätzel, M.; Durrant, J. R. Ultrafast Charge Carrier Recombination and Trapping in Hematite Photoanodes under Applied Bias. *J. Am. Chem. Soc.* **2014**, *136*, 9854−9857.

(38) Zhang, J.; Eslava, S. Understanding charge transfer, defects and surface states at hematite photoanodes. *Sustainable Energy Fuels* **2019**, *3*, 1351−1364.

(39) Hayes, D.; Hadt, R. G.; Emery, J. D.; Cordones, A. A.; Martinson, A. B. F.; Shelby, M. L.; Fransted, K. A.; Dahlberg, P. D.; Hong, J.; Zhang, X.; Kong, Q.; Schoenlein, R. W.; Chen, L. X. Electronic and nuclear contributions to time-resolved optical and X-ray absorption spectra of hematite and insights into photo-electrochemical performance. *Energy Environ. Sci.* **2016**, *9*, 3754−3769.

(40) Ruoko, T.-P.; Hiltunen, A.; Iivonen, T.; Ulkuniemi, R.; Lahtonen, K.; Ali-Löytty, H.; Mizohata, K.; Valden, M.; Leskelä, M.; Tkachenko, N. V. Charge carrier dynamics in tantalum oxide overlayered and tantalum doped hematite photoanodes. *J. Mater. Chem. A* **2019**, *7*, 3206−3215.

(41) Pyeon, M.; Ruoko, T.-P.; Leduc, J.; Gönüllü, Y.; Deo, M.; Tkachenko, N. V.; Mathur, S. Critical role and modification of surface states in hematite films for enhancing oxygen evolution activity. *J. Mater. Res.* **2018**, *33*, 455−466.

(42) Zandi, O.; Hamann, T. W. Enhanced Water Splitting Efficiency Through Selective Surface State Removal. *J. Phys. Chem. Lett.* **2014**, *5*, 1522−1526.

(43) Ling, Y.; Wang, G.; Wheeler, D. A.; Zhang, J. Z.; Li, Y. Sn-Doped Hematite Nanostructures for Photoelectrochemical Water Splitting. *Nano Lett.* **2011**, *11*, 2119−2125.

(44) Sohn, W. Y.; Thorne, J. E.; Zhang, Y.; Kuwahara, S.; Shen, Q.; Wang, D.; Katayama, K. Charge carrier kinetics in hematite with NiFeO$_x$ coating in aqueous solutions: Dependence on bias voltage. *J. Photochem. Photobiol., A* **2018**, *353*, 344−348.

(45) Sohn, W. Y.; Kuwahara, S.; Thorne, J. E.; Wang, D.; Katayama, K. Investigation of Photoexcited Carrier Dynamics in Hematite and the Effect of Surface Modifications by an Advanced Transient Grating Technique. *ACS Omega* **2017**, *2*, 1031−1035.